*Nano Research* 2018, 11(11): 5935–5945
https://doi.org/10.1007/s12274-018-2106-9
**Research Article**
ISSN 1998-0124
CN 11-5974/O4

# Towards high-mobility $In_{2x}Ga_{2-2x}O_3$ nanowire field-effect transistors

Ziyao Zhou[1,3], Changyong Lan[1,2], SenPo Yip[1,3,4], Renjie Wei[1,3], Dapan Li[1,3], Lei Shu[1,3,4], and Johnny C. Ho[1,3,4] (✉)

[1] *Department of Materials Science and Engineering, City University of Hong Kong, Kowloon, Hong Kong 999077, China*
[2] *School of Optoelectronic Science and Engineering, University of Electronic Science and Technology of China, Chengdu 610054, China*
[3] *Shenzhen Research Institute, City University of Hong Kong, Shenzhen 518057, China*
[4] *State Key Laboratory of Millimeter Waves, City University of Hong Kong, Kowloon, Hong Kong 999077, China*

**Received:** 7 March 2018
**Revised:** 26 April 2018
**Accepted:** 22 May 2018



**KEYWORDS**
$In_2O_3$, $In_{2x}Ga_{2-2x}O_3$,
nanowire,
chemical vapor deposition,
mobility,
oxygen vacancy

## ABSTRACT

Recently, owing to the excellent electrical and optical properties, n-type $In_2O_3$ nanowires (NWs) have attracted tremendous attention for application in memory devices, solar cells, and ultra-violet photodetectors. However, the relatively low electron mobility of $In_2O_3$ NWs grown by chemical vapor deposition (CVD) has limited their further utilization. In this study, utilizing *in-situ* Ga alloying, highly crystalline, uniform, and thin $In_{2x}Ga_{2-2x}O_3$ NWs with diameters down to 30 nm were successfully prepared via ambient-pressure CVD. Introducing an optimal amount of Ga (10 at.%) into the $In_2O_3$ lattice was found to effectively enhance the crystal quality and reduce the number of oxygen vacancies in the NWs. A further increase in the Ga concentration adversely induced the formation of a resistive β-$Ga_2O_3$ phase, thereby deteriorating the electrical properties of the NWs. Importantly, when configured into global back-gated NW field-effect transistors, the optimized $In_{1.8}Ga_{0.2}O_3$ NWs exhibit significantly enhanced electron mobility reaching up to 750 $cm^2 \cdot V^{-1} \cdot s^{-1}$ as compared with that of the pure $In_2O_3$ NW, which can be attributed to the reduction in the number of oxygen vacancies and ionized impurity scattering centers. Highly ordered NW parallel arrayed devices were also fabricated to demonstrate the versatility and potency of these NWs for next-generation, large-scale, and high-performance nanoelectronics, sensors, etc.

## 1 Introduction

In the past decades, because of the excellent chemical and physical properties, wide band gap oxide semiconductors have attracted extensive interest and are recognized as promising fundamental building blocks for next-generation electronics, gas sensors, optoelectronics, and others [1–9]. Particularly, as a

Address correspondence to johnnyho@cityu.edu.hk

technologically important n-type oxide semiconductor, more recent attention has been focused on indium oxide ($In_2O_3$) nanowire (NW) materials as compared with other oxide counterparts because of their unique electronic properties. For instance, fully transparent transistors based on single crystalline $In_2O_3$ NWs synthesized by pulsed laser deposition have been demonstrated with excellent field-effect electron mobilities ($\mu_e$), up to ~ 512 $cm^2 \cdot V^{-1} \cdot s^{-1}$ [10, 11]. However, although chemical vapor deposition (CVD) is widely recognized as an effective method for the large-scale and low-cost synthesis of nanomaterials, the transistor performance of $In_2O_3$ NWs enabled by ambient-pressure CVD via vapor-liquid-solid (VLS) growth mechanism still remains insufficient ($\mu_e$ ~ 200 $cm^2 \cdot V^{-1} \cdot s^{-1}$) for advanced applications [12–15]. This poor performance is mainly attributed to the uncontrollable radial growth (e.g., overgrowth) leading to the growth of thick and non-uniform $In_2O_3$ NWs induced by the well-known Gibbs–Thomson effect, especially, the observation of unfavorable nanostructures such as zig-zag, nanocrystal chains, and networks of NWs [16–22]. Furthermore, there are always a large number of oxygen vacancies within the $In_2O_3$ NWs and these oxygen vacancies could act as impurity scatter centers, thereby deteriorating the transport of carriers and hindering the electrical performance of the subsequently fabricated NW devices [14, 20, 23]. Therefore, it is challenging to achieve high-quality thin $In_2O_3$ NWs with controllable diameters and less oxygen vacancies via the CVD growth.

At the same time, previous works have reported the key role of Ga alloying or doping in the synthesis process and its influence on the electrical properties of indium gallium zinc oxide thin-films and zinc oxide NW-based transistors [24–27]. Ga alloying is shown to effectively enable the synthesis of thin and ultra-thin oxide semiconductors to achieve high-quality oxide-lattice structures during their synthesis [28–30]. As compared with the In atoms, the atomic Ga can minimize the formation of intrinsic defects such as oxygen vacancies, because Ga has a relatively higher binding energy with oxygen atom and preferentially forms stronger chemical bonds with it [31, 32]. In this case, the incorporation of Ga into the $In_2O_3$ lattice is anticipated to improve the bonding of oxygen with cations and correspondingly reduce the defect density (e.g., number of oxygen vacancies); however, there are still very limited studies on exploring reliable Ga alloying to achieve $In_{2x}Ga_{2-2x}O_3$ nanostructures, which may provide important information for achieving further improvement in the device performance.

Here, we introduce controllable *in-situ* Ga alloying into $In_2O_3$ to attain crystalline and uniform $In_{2x}Ga_{2-2x}O_3$ NWs with diameters in the range of 20–40 nm via ambient-pressure CVD. In specific, the incorporation of Ga atoms into the $In_2O_3$ lattice is found to suppress the uneven radial NW growth, to improve the NW crystallinity and more importantly to reduce the formation of oxygen vacancies. With optimal Ga alloying (10 at.%), when configured into field-effect transistors (FETs), the single $In_{1.8}Ga_{0.2}O_3$ NW and the parallel NW arrays exhibit much improved peak electron mobilities with maximum values of up to 750 and 210 $cm^2 \cdot V^{-1} \cdot s^{-1}$, respectively. The device threshold voltage ($V_{th}$) is also observed to shift towards the positive direction with increasing Ga concentration, which indicates the slight decrease in the free electron concentration, being consistent with the reduction in the donor-like oxygen vacancies. All these results would provide valuable insights for achieving high-performance $In_2O_3$ NWs by *in-situ* Ga alloying for advanced electronic and optoelectronic applications.

## 2 Experimental section

### 2.1 Nanowire synthesis

$Si/SiO_2$ (50-nm-thick thermally grown oxide) substrates with a layer of 0.1 nm (nominal thickness) Au film pre-deposited by thermal evaporation was used for the growth of $In_2O_3$ and $In_{2x}Ga_{2-2x}O_3$ NWs by the ambient-pressure CVD method. For the growth of $In_2O_3$ NWs, 1.5 g of high-purity In metal granules (1–2 mm in size; 99.999%; China Rare Metal) was used as the In source. For the growth of $In_{2x}Ga_{2-2x}O_3$ NWs, the metal granules of Ga and In (1–2 mm in size; 99.999%; China Rare Metal) were used at different molar ratios (e.g., 3:1 for $In_{1.8}Ga_{0.2}O_3$, 1:1 for $In_{1.52}Ga_{0.48}O_3$, and 1:3 for $In_{0.66}Ga_{1.34}O_3$ NWs; 1.5 g of

the source materials in total for each growth) in order to control the stoichiometry of the NWs. Further, 0.5 g of a graphite powder (< 20 μm in size, synthetic; Sigma-Aldrich) was mixed with the metal source as the precursor. During the growth, the precursor mixture was placed at the sealed end whereas the substrate was positioned at the open end of a small quartz tube (10 cm in length and 1 cm in diameter). The entire set-up was then placed in the center of a large quartz tube (1 inch in diameter), located in a single-zone horizontal tube furnace. Next, a mixed gas of 4% oxygen (99.999%) and 96% argon (99.9995%) was introduced as the carrier gas into the quartz tube. The furnace was heated to 1,030 ℃ in 30 min, held for 30 min, and then cooled to room temperature naturally. After the synthesis, a fluffy white product was found on the substrate. The growth was also noted to be highly sensitive to the temperature. When the temperature was set below 1,030 ℃, no NW was obtained. Once the temperature was adjusted to > 1,030 ℃, significant coatings were observed on the NWs.

### 2.2 Material characterization

The crystal structures of the obtained NWs were determined by X-ray diffraction (XRD) performed on a powder X-ray diffractometer (RIGAKU, Philips) using Cu K$\alpha$ radiation ($\lambda$ = 1.5406 Å). The NW morphologies were examined using a scanning electron microscope (SEM, XL30, FEI) and transmission electron microscope (TEM, Tecnai F30, FEI). High-resolution TEM (HRTEM) observations and selected area electron diffraction (SAED) were also performed to assess the crystal structure and crystallinity of the NWs. For the TEM studies, the NWs were first suspended in ethanol by ultrasonication and then drop-casted onto TEM Cu grids. The chemical composition of the NWs was determined using an energy dispersive X-ray spectrometer (EDS) attached to the SEM and TEM. The corresponding EDS mappings were also obtained from EDS attached to TEM.

### 2.3 Single NW FET fabrication and electrical measurement

After the growth, the NWs were drop-casted onto degenerately boron-doped Si substrates with a 50-nm-thick thermally grown gate oxide layer on top. Photolithography was utilized to define the source and drain regions, and 5/80-nm thick Ti/Au film was deposited by electron beam evaporation followed by a lift-off process to serve as the contact electrodes. The electrical performance of the fabricated back-gate FETs was then evaluated using a standard electrical probe station with an Agilent 4155C semiconductor analyzer (Agilent Technologies, Santa Clara, CA, USA).

## 3 Results and discussion

As shown in the SEM images in Figs. 1(a) and 1(b), both $In_2O_3$ and Ga-alloyed $In_2O_3$ (e.g., $In_{1.8}Ga_{0.2}O_3$) products have wire-like morphology with lengths of tens of micrometers. However, the distribution of the diameters of the NWs in the two samples is very different although the same catalyst film thickness was utilized for the growth. The NW diameter is found to be significantly reduced after Ga alloying. In order to understand the difference, statistical distributions of the NW diameters of $In_2O_3$ and $In_{1.8}Ga_{0.2}O_3$ were evaluated and the results are presented in Fig. 1(c); the diameters were extracted from the TEM images of the NWs. It is clear that the diameter of $In_2O_3$ NWs is 96 ± 23 nm, whereas the

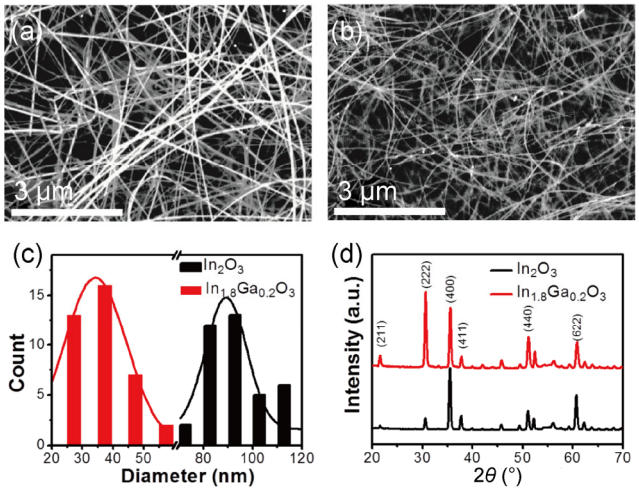


**Figure 1** Morphology, diameter distribution, and crystal structure of as-prepared $In_2O_3$ NWs and $In_{1.8}Ga_{0.2}O_3$ NWs. (a) SEM image of $In_2O_3$ NWs. (b) SEM image of $In_{1.8}Ga_{0.2}O_3$ NWs. (c) Histogram for the diameter distribution with Gaussian fitting performed. (d) XRD patterns of the obtained NWs.

diameter of $In_{1.8}Ga_{0.2}O_3$ NWs is 32 ± 12 nm, which is ~ 3 times smaller than that of pure $In_2O_3$ NWs. Further, once Ga atoms are introduced into the $In_2O_3$ lattice, the NW diameter is decreased substantially and remains relatively constant as the Ga concentration is increased further up to 67 at.% (data not shown). It is also noted that, on average, the $In_{1.8}Ga_{0.2}O_3$ NWs are much longer than the $In_2O_3$ NWs. Specifically, the longitudinal growth rates of $In_2O_3$ and $In_{1.8}Ga_{0.2}O_3$ NWs were qualitatively estimated as 0.9 and 2.1 μm·min$^{-1}$, respectively (Fig. S1 in the Electronic Supplementary Material (ESM)). The presence of Ga would typically decrease the vapor pressure of the corresponding metal oxides, leading to a higher longitudinal growth rate [33, 34]. Based on the well-known Gibbs–Thomson effect, the observed increase in the longitudinal growth rate usually leads to smaller diameters of the NWs grown via the VLS mechanism [35, 36]. All these results evidently indicate that Ga alloying can effectively prevent the radial growth to yield thin and uniform NWs. At the same time, EDS was performed to assess the chemical composition of the obtained NWs. Figure S2 in the ESM displays a typical EDS spectrum of NWs grown with the specific precursor mixing ratio of 3:1 (In:Ga), in which the In, Ga, and O signals are clearly observed with the elemental ratio of 1:0.11:2.31, indicating the stoichiometry of the NW being $In_{1.8}Ga_{0.2}O_3$ with 10 at.% Ga alloying. XRD was then carried out to evaluate the crystal structure of the NWs. As depicted in Fig. 1(d), all the diffraction peaks can be indexed to cubic $In_2O_3$ (JCPDS Card No. 06-0416), suggesting the phase purity of $In_2O_3$ and $In_{1.8}Ga_{0.2}O_3$ NWs [18, 37]. The high phase purity suggests the absence of any other impurity phase. In the high-resolution XRD patterns (Fig. S3 in the ESM), the (400) peak of $In_2O_3$ is observed to shift to higher angles, from 35.50° to 35.57°, after Ga alloying, indicating the incorporation of Ga into the lattice of $In_2O_3$. However, upon increasing the Ga concentration further to more than 24 at.%, additional peaks associated with β-$Ga_2O_3$ start to appear, revealing the phase segregation between $In_2O_3$ and β-$Ga_2O_3$ within the NWs (Fig. S4 in the ESM).

In addition, the surface morphology of the obtained NWs could be confirmed by detailed TEM characterization, as illustrated in Figs. 2(a) and 2(b). It is obvious that the typical diameter of $In_2O_3$ NWs is 80 nm, whereas the representative diameter of $In_{1.8}Ga_{0.2}O_3$ NWs is 28 nm. The reduced NW diameter after Ga alloying is perfectly consistent with the SEM results. The single-crystalline nature of the $In_2O_3$ and $In_{1.8}Ga_{0.2}O_3$ NWs could also be confirmed by the SAED patterns (see the inset of Figs. 2(a) and 2(b), respectively). From the SAED patterns, the growth direction of both $In_2O_3$ and $In_{1.8}Ga_{0.2}O_3$ NWs is found to be the same, which is along the [110] direction [11, 16], suggesting that Ga alloying up to 10 at.% does not have any noticeable impact on the lattice structure owing to the small difference between the atomic radius of Ga and In as well as the high compatibility of Ga atoms with the cubic structure of $In_2O_3$. The excellent crystallinity of the NW is also evidenced by the clear lattice fringes shown in Figs. 2(c) and 2(d). In specific, the lattice spacing of $In_2O_3$ is measured to be 0.255 nm, corresponding to the {400} planes of cubic $In_2O_3$. The lattice spacing of $In_{1.8}Ga_{0.2}O_3$ for the same plane is slightly smaller at 0.243 nm,

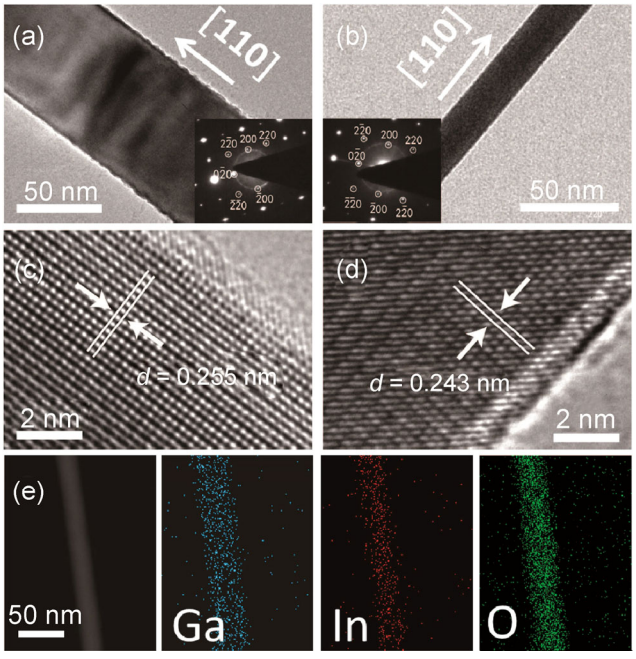


**Figure 2** TEM characterization and elemental analysis. (a) and (b) TEM images and the corresponding SAED patterns with the zone axis of [001] (inset) of representative $In_2O_3$ NWs and $In_{1.8}Ga_{0.2}O_3$ NWs, respectively. (c) and (d) HRTEM images of $In_2O_3$ and $In_{1.8}Ga_{0.2}O_3$ NWs, respectively. (e) Scanning TEM image of the $In_{1.8}Ga_{0.2}O_3$ NW with the elemental mapping of Ga, In, and O, respectively.

because of the smaller atomic radius of Ga than that of In [24]. To investigate the uniformity of the distribution of the constituents in $In_{1.8}Ga_{0.2}O_3$ NWs, the corresponding EDS mapping was performed (Fig. 2(e)). It is evident that Ga, In, and O are homogenously distributed along the NW. All these results suggest that Ga is uniformly distributed in the $In_2O_3$ lattice, without any significant segregation and defect formation.

Apart from the excellent crystallinity and uniform elemental distribution, it is important to determine the electrical property of these $In_{2x}Ga_{2-2x}O_3$ NWs. In this study, single NW and parallel NW array-based devices configured in the global back-gated geometry were employed; an illustrative schematic of the device and the corresponding SEM image are shown in the inset of Fig. 3(a). Based on the typical transfer characteristics of both single $In_2O_3$ and $In_{1.8}Ga_{0.2}O_3$ NW devices (Fig. 3(a)), it is clear that the source-drain current ($I_{ds}$) increases with increasing back-gate voltage ($V_{gs}$), indicating the n-type conducting behaviors of both types of NWs. In specific, the $In_2O_3$ and $In_{1.8}Ga_{0.2}O_3$ NWFETs deliver ~ 25 and ~ 30 μA on-current under $V_{ds}$ = 1 V and $V_{gs}$ = 20 V, respectively. The hysteresis in the transfer characteristics is possibly induced by the contamination of the nanowire surface or the gate oxide in the proximity of the nanowire, moveable ions in the dielectric, absorbents from air, etc. Further, the linear $I_{ds}$–$V_{ds}$ relationship in the output characteristics further confirms the nearly ohmic contact between the NWs and the electrodes (Fig. 3(b)). The free carrier concentration ($n$) of the as-synthesized NWs can be extracted from the transfer curves in Fig. 3(a) using Eq. (1)

$$n = \left| \frac{4C_{ox}V_{th}}{\pi q d^2 L} \right| \quad (1)$$

where, $C_{ox}$ is the gate capacitance that can be accurately obtained from the finite element analysis software COMSOL, $V_{th}$ is the threshold voltage, $q$ is the charge

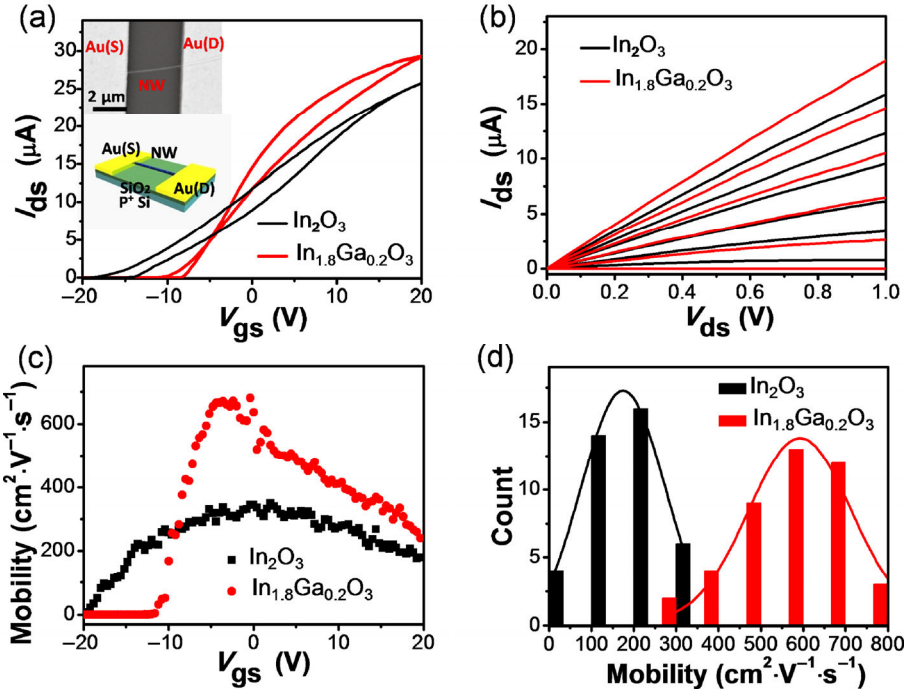


**Figure 3** Electrical characterization of typical FETs fabricated with $In_2O_3$ and $In_{1.8}Ga_{0.2}O_3$ NWs. (a) Transfer characteristics of two representative back-gated FETs based on single $In_2O_3$ and $In_{1.8}Ga_{0.2}O_3$ NWs, respectively ($V_{ds}$ = 1 V). The inset shows the SEM image of the FET with 3-μm channel length fabricated with the $In_{1.8}Ga_{0.2}O_3$ NW and the schematic illustration of the device. The scale bar is 1 μm. (b) Corresponding output characteristics of the NWFET under $V_{gs}$ = −10, −7, −4, −1, 2, and 5 V from bottom to top. (c) Field-effect electron mobility assessment for the same set of FETs presented in (a) with $V_{ds}$ = 1 V. (d) Statistical results of the peak field-effect electron mobility of ~ 80 FETs based on $In_2O_3$ and $In_{1.8}Ga_{0.2}O_3$ NWs. Gaussian fitting is performed on the histogram.

of an electron, $d$ is the diameter of the NW, and $L$ is the length of the FET channel [21, 23]. As compared with the device based on the $In_2O_3$ NW channel, the $In_{1.8}Ga_{0.2}O_3$ NWFET exhibits a lower carrier concentration at the zero gate voltage and the $n$ value decreases from $1.21 \times 10^{19}$ to $1.05 \times 10^{19}$ $cm^{-3}$, accordingly. At the same time, the $\mu_e$ of single NW FET can also be calculated from the transfer curves using Eq. (2), as presented in Fig. 3(c) [38, 39].

$$\mu_e = \frac{g_m L^2}{C_{ox} V_{ds}} \quad (2)$$

Here, $g_m$ is the transconductance, which is $dI_{ds}/dV_{gs}$. Thus, the peak $\mu_e$ values of the $In_2O_3$ and $In_{1.8}Ga_{0.2}O_3$ NW devices are found to be 320 and 700 $cm^2 \cdot V^{-1} \cdot s^{-1}$, respectively. It is obvious that the electron mobility of the $In_{1.8}Ga_{0.2}O_3$ NW FET is more than twice of that of pure $In_2O_3$ NW, indicating that Ga alloying at 10 at.% is beneficial for enhancing the performance of the $In_2O_3$ NW electronic device. To further confirm this trend, statistical distributions of the mobilities of more than 30 $In_2O_3$ and $In_{1.8}Ga_{0.2}O_3$ NW devices with similar NW diameters were collected for each sample group, as depicted Fig. 3(d). Evidently, the average mobility (590 $cm^2 \cdot V^{-1} \cdot s^{-1}$) of $In_{1.8}Ga_{0.2}O_3$ NW devices is more than twice that of pure $In_2O_3$ NW devices (210 $cm^2 \cdot V^{-1} \cdot s^{-1}$), confirming the enhancement of the electron mobility simply through Ga alloying. The slight variation between the peak mobility and average mobility can be attributed to the dependence of the electrical properties on the NW crystallinity, surface roughness, and many other factors.

To shed light on the enhancement of the electron mobility of $In_{1.8}Ga_{0.2}O_3$ NW devices, X-ray photoelectron spectroscopy (XPS) was carried out. As shown in Figs. 4(a) and 4(b), the In 4d peak and the O 1s peaks of pure $In_2O_3$ NWs are clearly observed in the XPS spectra. For $In_{1.8}Ga_{0.2}O_3$ NWs, apart from the In 4d and O 1s peaks, the Ga 3d peak is also observed (Fig. 4(c)), indicating the incorporation of Ga in the $In_2O_3$ NWs. Further, there is a tiny shift of the In 4d peak as compared with that of pure $In_2O_3$ NWs, which may be attributed to the size effect, as reported in the literature [40, 41]. Interestingly, the XPS peak profile of O 1s of $In_{1.8}Ga_{0.2}O_3$ NWs is substantially different from that of pure $In_2O_3$ NWs, as shown in Figs. 4(b) and 4(d). Specifically, Gaussian fittings of the peak profiles were made to clearly illustrate the

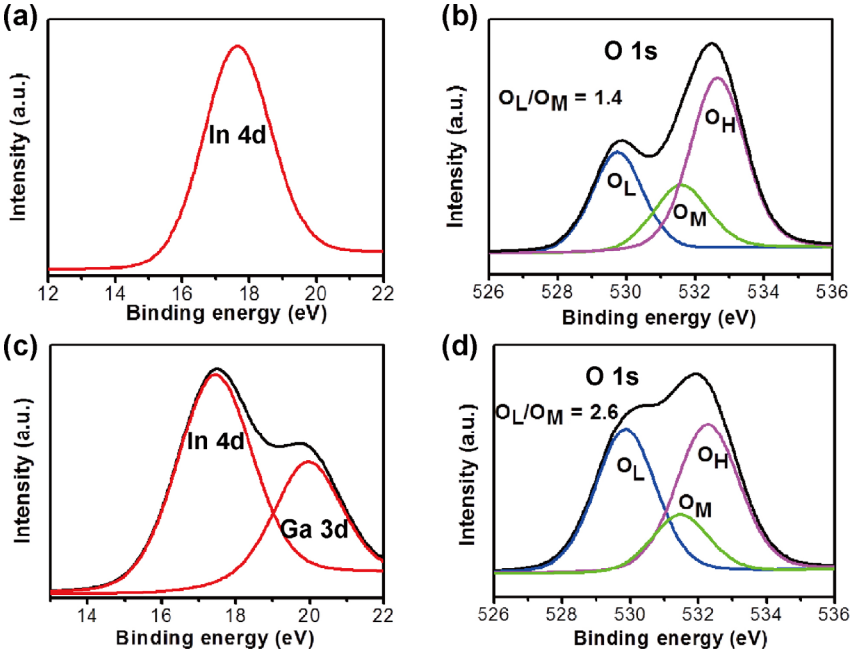


**Figure 4** XPS characterization of the obtained NWs. XPS spectra of the In 4d, Ga 3d, and O 1s levels of $In_2O_3$ NWs (a) and (b) and $In_{1.8}Ga_{0.2}O_3$ NWs (c) and (d). Gaussian-resolved fitting curves labeled as $O_L$, $O_M$, and $O_H$, designating the $O^{2-}$ ions in the cubic structure, $O^{2-}$ ions in the oxygen deficient region, and loosely bound oxygen atoms on the surface, respectively.

observed difference. The component labeled as $O_H$ located at 532.25 ± 0.2 eV, with a higher binding energy, is usually attributed to the presence of loosely bound oxygen on the surface of NWs, belonging to some chemisorbed species such as adsorbed $H_2O$ or $O_2$. The medium binding energy component at 530.8 ± 0.15 eV, labeled as $O_M$, is related to the $O^{2-}$ ions that are in the oxygen-deficient regions within the $In_2O_3$ matrix [30, 42, 43]. Therefore, the changes in the intensity of this component are usually associated with the variation in the concentration of the oxygen defects. The component at the lower binding energy (529.6 ± 0.2 eV), labeled as $O_L$, represents the $O^{2-}$ ions located in the substitutional sites of the $In_2O_3$ lattice; these are surrounded by In ions with their full complement of the nearest neighbor $O^{2-}$ ions. In other words, the intensity of this component can simply be a measure of the number of oxygen atoms located in the substitutional sites, with fully oxidized stoichiometry. At the same time, to further analyze the relationship between different components of the O 1s peak, the area ratio of $O_L/O_M$ in $In_2O_3$ and $In_{1.8}Ga_{0.2}O_3$ NWs were determined to be 1.4 and 2.6, respectively. This result indicates that the number of oxygen vacancies of $In_{1.8}Ga_{0.2}O_3$ NWs is qualitatively smaller than that of pure $In_2O_3$ NWs. Since the Ga–O bonds are typically stronger than the In–O bonds in terms of their bond energies, the optimal Ga alloying in $In_2O_3$ NWs can improve the effectiveness of oxygen bonding with metal constituents and hence decreases the density of oxygen vacancies there. Explicitly, the free electron generation can be closely related to the substitution of oxygen according to the following equation [28].

$$O_o^x = \frac{1}{2}O_2 + V_o^{\bullet\bullet} + 2e^- \quad (3)$$

Here, the $O_2$ species can be formed by O atoms from the oxide sublattice. The doubly positively charged oxygen vacancy and two free electrons are also created in the same process, indicating that the decrease in the free electron concentration is merely a result of the reduction in the number of oxygen vacancies. Furthermore, the oxygen vacancies can as well act as ionized impurity scattering centers and have a predominant effect on the electron mobility of the NWs. As a result, the reduction in the number of oxygen vacancies would lead to a slight decrease in the free electron concentration and enhanced electron mobility of $In_{1.8}Ga_{0.2}O_3$ NWs as compared with those of their pure $In_2O_3$ counterparts.

In order to demonstrate the potential application of these $In_{1.8}Ga_{0.2}O_3$ NWs, large-scale NW parallel arrayed FETs were then fabricated via the well-established NW contact printing technique (Fig. 5(a)) [19, 44]. It is clear that an impressive on/off current ratio of $10^5$ could be achieved (Fig. 5(b)). The linear relation of the $I_{ds}$ vs. $V_{ds}$ curves also confirms the nearly ohmic contact between the electrodes and the NWs (Fig. 5(c)). Considering the channel width of 100 μm, the device outputs a current density of ~ 10 μA·μm$^{-1}$ under $V_{ds}$ = 2 V and $V_{gs}$ = 30 V. This current density can be further enhanced by increasing the NW print density in the device. Further, the corresponding field-effect electron mobility of the device was also evaluated using Eq. (2). For these NW arrayed devices, the capacitance is calculated by multiplying the electrostatically modeled gate oxide capacitance for a single NW by the number of NWs in the arrayed device. The extracted peak electron mobility is 210 cm$^2$·V$^{-1}$·s$^{-1}$ (Fig. 5(d)). All these performance data are comparable or even better than those of other state-of-the-art n-type thin-film oxide transistors reported in the literature [45, 46]. However, as compared with the single $In_{1.8}Ga_{0.2}O_3$ NW device (Fig. 3(a)), the performance (e.g., output current density, electron mobility, etc.) of the NW parallel arrayed device seems to deteriorate, which is probably due to the inefficient electrical contact between the NWs and electrodes as well as the ineffective gate coupling owing to the slight misalignment of the printed NW arrays. Inevitably, some fragmented wires would also exist within the channel, which increase the parasitic capacitance and deteriorate the device performance. In the future, this performance can be enhanced by down-scaling the channel length, optimizing the NW printing, and adopting a top-gate device structure with high-dielectrics. Moreover, it is also critical to investigate the effect of the Ga concentration on the electrical properties of the $In_{2x}Ga_{2-2x}O_3$ NW devices (Fig. S5 in the ESM). As discussed above, a higher Ga concentration reduced

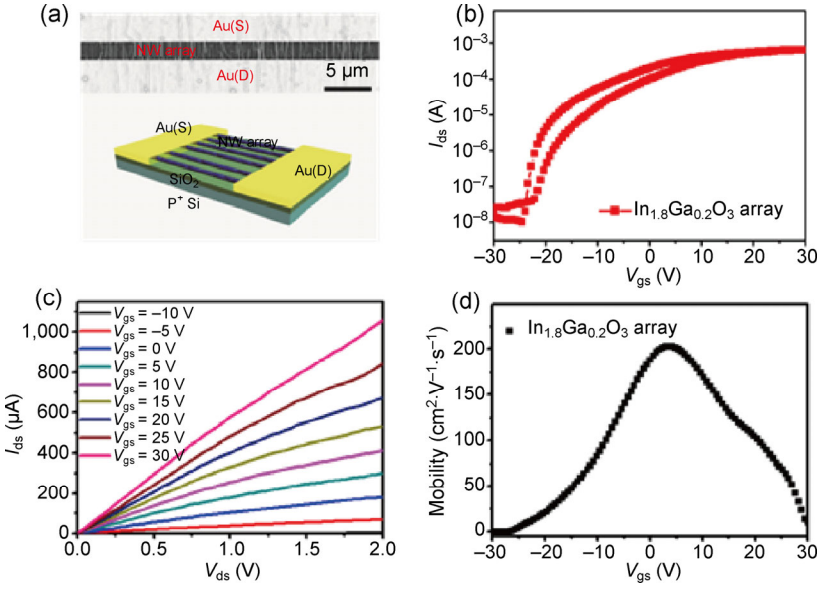


**Figure 5** Electrical characterization of the fabricated $In_{1.8}Ga_{0.2}O_3$ NW parallel arrayed devices. (a) (Top) Typical SEM image and (bottom) illustrative schematic of a contact-printed back-gated NW parallel arrayed FET with Au electrodes. (b) Transfer curves of the device (channel length = 2.5 μm; channel width = 100 μm; $V_{ds}$ = 2 V). (c) Output curves of the device. (d) Corresponding field-effect electron mobility assessed as a function of gate voltage bias at $V_{ds}$ = 2 V.

the free electron concentration, owing to the formation of an additional phase of β-$Ga_2O_3$ and corresponding phase segregation between $In_2O_3$ and β-$Ga_2O_3$ of the NWs. In this case, as anticipated, with an increase in the Ga concentration from 10 at.% to 67 at.%, the average $V_{th}$ value increases from approximately −14 to 4 V, accordingly (Fig. 6(a)). Meanwhile, the output current first increases from 25.4 to 29.3 μA and then drops continuously to 10.1 and 2.5 μA (Fig. 6(b)), while the $I_{on}/I_{off}$ ratio changes with a similar tendency as

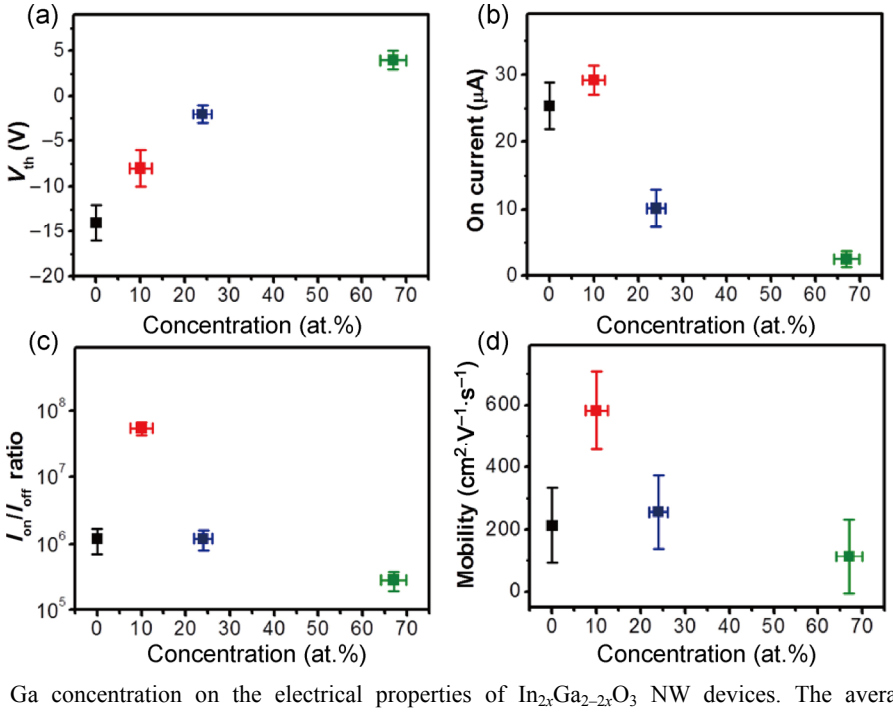


**Figure 6** Effect of Ga concentration on the electrical properties of $In_{2x}Ga_{2-2x}O_3$ NW devices. The average value of (a) $V_{th}$, (b) on-current, (c) $I_{on}/I_{off}$ ratio, and (d) peak mobility extracted from more than 40 NW FETs fabricated with pure $In_2O_3$ and 10 at.%, 24 at.%, and 67 at.% Ga-alloyed $In_2O_3$ NWs, respectively.

that of the output current, being significantly improved from $1.2 \times 10^6$ to $5.5 \times 10^7$, and then drops continuously to $1.0 \times 10^6$ and $2.8 \times 10^5$ (Fig. 6(c)). Importantly, owing to the better crystallinity and the reduction of impurity scattering centers induced by Ga alloying, the average value of the peak electron mobility increases from 218 to 582 $cm^2 \cdot V^{-1} \cdot s^{-1}$ with an increase in the Ga concentration up to 10 at.%, and then decreases to 257 and 114 $cm^2 \cdot V^{-1} \cdot s^{-1}$, with further increase in the Ga concentration (Fig. 6(d)). This decline in $\mu_e$ is mainly caused by precipitation or formation of the β-$Ga_2O_3$ phase, when the Ga concentration reaches the supersaturation limit within the $In_2O_3$ lattice; the existence of β-$Ga_2O_3$ domains would be detrimental to the electrical properties of the NWs owing to their poor electrical conductivity. As a result, the enhanced electrical characteristic of $In_{2x}Ga_{2-2x}O_3$ NWs is achieved at the optimal Ga concentration for various technological applications.

## 4 Conclusions

Crystalline and uniform $In_{2x}Ga_{2-2x}O_3$ NWs were successfully synthesized by ambient-pressure CVD. The Ga concentration plays an important role in the synthesis process and has a great impact on the electrical properties of the obtained NWs, owing to the higher binding energy of Ga with oxygen atoms. In specific, incorporating Ga into the $In_2O_3$ lattice is found to be effective for controlling the non-uniform NW radial growth and minimizing the growth of unfavorable nanostructures of $In_2O_3$. Furthermore, the XPS data reveals that the optimal Ga concentration of 10 at.% (i.e., $In_{1.8}Ga_{0.2}O_3$) would lead to the reduction of oxygen vacancies in $In_2O_3$ NWs. This optimal Ga concentration also yields enhanced peak electron mobility reaching up to 750 $cm^2 \cdot V^{-1} \cdot s^{-1}$ when a global back-gated NW device is fabricated and evaluated. When the Ga concentration was increased further, the NW device performance deteriorated, probably owing to the precipitation or formation of the β-$Ga_2O_3$ phase with higher resistivity. More importantly, as compared with other conventional n-type thin-film oxide transistors, the NW parallel arrayed device exhibits superior performance with peak electron mobility of 210 $cm^2 \cdot V^{-1} \cdot s^{-1}$ and current density of 10 $\mu A \cdot \mu m^{-1}$. All these results demonstrate the great potential of these NWs for next-generation, large-scale, and high-performance nanoelectronics, sensors, etc.

## Acknowledgements

We acknowledge the General Research Fund (No. CityU 11275916) and the Theme-based Research Scheme (No. T42-103/16-N) of the Research Grants Council of Hong Kong SAR, China, the National Natural Science Foundation of China (Nos. 51672229 and 61605024), the Science Technology and Innovation Committee of Shenzhen Municipality (No. JCYJ20160229165240684) and a grant from the Shenzhen Research Institute, City University of Hong Kong.

**Electronic Supplementary Material**: Supplementary material (cross section of SEM of as-prepared $In_2O_3$ NWs and $In_{1.8}Ga_{0.2}O_3$ NWs, EDS spectra of the NWs of $In_{1.8}Ga_{0.2}O_3$ NWs, XRD data of as-prepared $In_{1.52}Ga_{0.48}O_3$ and $In_{0.66}Ga_{1.34}O_3$ NWs, and electrical characterization of back-gate FETs based on single $In_2O_3$, $In_{1.8}Ga_{0.2}O_3$, $In_{11.52}Ga_{0.48}O_3$ and $In_{0.66}Ga_{1.34}O_3$ NWs) is available in the online version of this article at https://doi.org/10.1007/s12274-018-2106-9.

## References

[1] Liu, Q. Z.; Liu, Y. H.; Wu, F. Q.; Cao, X.; Li, Z.; Alharbi, M.; Abbas, A. N.; Amer, M. R.; Zhou, C. W. Highly sensitive and wearable $In_2O_3$ nanoribbon transistor biosensors with integrated on-chip gate for glucose monitoring in body fluids. *ACS Nano* **2018**, *12*, 1170–1178.

[2] Meng, M.; Wu, X. L.; Ji, X. L.; Gan, Z. X.; Liu, L. Z.; Shen, J. C.; Chu, P. K. Ultrahigh quantum efficiency photodetector and ultrafast reversible surface wettability transition of square $In_2O_3$ nanowires. *Nano Res.* **2017**, *10*, 2772–2781.

[3] Macco, B.; Knoops, H. C. M.; Kessels, W. M. M. Electron scattering and doping mechanisms in solid-phase-crystallized $In_2O_3$:H prepared by atomic layer deposition. *ACS Appl. Mater. Interfaces* **2015**, *7*, 16723–16729.

[4] Park, S.; Kim, S.; Sun, G.-J.; Lee, C. Synthesis, structure, and ethanol gas sensing properties of $In_2O_3$ nanorods decorated with $Bi_2O_3$ nanoparticles. *ACS Appl. Mater. Interfaces* **2015**, *7*, 8138–8146.

[5] Liu, A.; Liu, G. X.; Zhu, H. H.; Xu, F.; Fortunato, E.; Martins, R.; Shan, F. K. Fully solution-processed low-voltage aqueous $In_2O_3$ thin-film transistors using an ultrathin $ZrO_x$

dielectric. *ACS Appl. Mater. Interfaces* **2014**, *6*, 17364–17369.

[6] Khim, D.; Lin, Y.-H.; Nam, S.; Faber, H.; Tetzner, K.; Li, R. P.; Zhang, Q.; Li, J.; Zhang, X. X.; Anthopoulos, T. D. Modulation-doped $In_2O_3$/ZnO heterojunction transistors processed from solution. *Adv. Mater.* **2017**, *29*, 1605837.

[7] Leppäniemi, J.; Huttunen, O.-H.; Majumdar, H.; Alastalo, A. Flexography-printed $In_2O_3$ semiconductor layers for high-mobility thin-film transistors on flexible plastic substrate. *Adv. Mater.* **2015**, *27*, 7168–7175.

[8] Kim, J.; Rim, Y. S.; Chen, H. J.; Cao, H. H.; Nakatsuka, N.; Hinton, H. L.; Zhao, C. Z.; Andrews, A. M.; Yang, Y.; Weiss, P. S. Fabrication of high-performance ultrathin $In_2O_3$ film field-effect transistors and biosensors using chemical lift-off lithography. *ACS Nano* **2015**, *9*, 4572–4582.

[9] Hou, J. G.; Cao, S. Y.; Sun, Y. Q.; Wu, Y. Z.; Liang, F.; Lin, Z. S.; Sun, L. C. Atomically thin mesoporous $In_2O_{3-x}$/$In_2S_3$ lateral heterostructures enabling robust broadband-light photo-electrochemical water splitting. *Adv. Energy Mater.* **2018**, *8*, 1701114.

[10] Ju, S.; Facchetti, A.; Xuan, Y.; Liu, J.; Ishikawa, F.; Ye, P. D.; Zhou, C. W.; Marks, T. J.; Janes, D. B. Fabrication of fully transparent nanowire transistors for transparent and flexible electronics. *Nat. Nanotechnol.* **2007**, *2*, 378–384.

[11] Li, C.; Zhang, D.; Han, S.; Liu, X.; Tang, T.; Zhou, C. Diameter-controlled growth of single-crystalline $In_2O_3$ nanowires and their electronic properties. *Adv. Mater.* **2003**, *15*, 143–146.

[12] Zou, X. M.; Liu, X. Q.; Wang, C. L.; Jiang, Y.; Wang, Y.; Xiao, X. H.; Ho, J. C.; Li, J. C.; Jiang, C. Z.; Xiong, Q. H. et al. Controllable electrical properties of metal-doped $In_2O_3$ nanowires for high-performance enhancement-mode transistors. *ACS Nano* **2013**, *7*, 804–810.

[13] Shen, G. Z.; Xu, J.; Wang, X. F.; Huang, H. T.; Chen, D. Growth of directly transferable $In_2O_3$ nanowire mats for transparent thin-film transistor applications. *Adv. Mater.* **2011**, *23*, 771–775.

[14] Lei, B.; Li, C.; Zhang, D.; Tang, T.; Zhou, C. Tuning electronic properties of $In_2O_3$ nanowires by doping control. *Appl. Phys. A* **2004**, *79*, 439–442.

[15] Peng, X. S.; Wang, Y. W.; Zhang, J.; Wang, X. F.; Zhao, L. X.; Meng, G. W.; Zhang, L. D. Large-scale synthesis of $In_2O_3$ nanowires. *Appl. Phys. A* **2002**, *74*, 437–439.

[16] Lao, J.; Huang, J.; Wang, D.; Ren, Z. Self-assembled $In_2O_3$ nanocrystal chains and nanowire networks. *Adv. Mater.* **2004**, *16*, 65–69.

[17] Yan, Y. G.; Zhang, Y.; Zeng, H. B.; Zhang, J. X.; Cao, X. L.; Zhang, L. D. Tunable synthesis of $In_2O_3$ nanowires, nano-arrows and nanorods. *Nanotechnology* **2007**, *18*, 175601.

[18] Kam, K. C.; Deepak, F. L.; Cheetham, A. K.; Rao, C. N. R. $In_2O_3$ nanowires, nanobouquets and nanotrees. *Chem. Phys. Lett.* **2004**, *397*, 329–334.

[19] Han, N.; Yang, Z. X.; Wang, F. Y.; Yip, S.; Dong, G. F.; Liang, X. G.; Hung, T.; Chen, Y. F.; Ho, J. C. Modulating the morphology and electrical properties of GaAs nanowires via catalyst stabilization by oxygen. *ACS Appl. Mater. Interfaces* **2015**, *7*, 5591–5597.

[20] Zhang, D. H.; Ma, H. L. Scattering mechanisms of charge carriers in transparent conducting oxide films. *Appl. Phys. A* **1996**, *62*, 487–492.

[21] Yang, Z.-X.; Yip, S.; Li, D. P.; Han, N.; Dong, G. F.; Liang, X. G.; Shu, L.; Hung, T. F.; Mo, X. L.; Ho, J. C. Approaching the hole mobility limit of GaSb nanowires. *ACS Nano* **2015**, *9*, 9268–9275.

[22] Shen, Y. D.; Chen, R. J.; Yu, X. C.; Wang, Q. J.; Jungjohann, K. L.; Dayeh, S. A.; Wu, T. Gibbs–Thomson effect in planar nanowires: Orientation and doping modulated growth. *Nano Lett.* **2016**, *16*, 4158–4165.

[23] Li, W. Q.; Liao, L.; Xiao, X. H.; Zhao, X. Y.; Dai, Z. G.; Guo, S. S.; Wu, W.; Shi, Y.; Xu, J. X.; Ren, F. et al. Modulating the threshold voltage of oxide nanowire field-effect transistors by a $Ga^+$ ion beam. *Nano Res.* **2014**, *7*, 1691–1698.

[24] Nomura, K.; Ohta, H.; Takagi, A.; Kamiya, T.; Hirano, M.; Hosono, H. Room-temperature fabrication of transparent flexible thin-film transistors using amorphous oxide semiconductors. *Nature* **2004**, *432*, 488–492.

[25] Yuan, G. D.; Zhang, W. J.; Jie, J. S.; Fan, X.; Tang, J. X.; Shafiq, I.; Ye, Z. Z.; Lee, C. S.; Lee, S. T. Tunable n-type conductivity and transport properties of Ga-doped ZnO nanowire arrays. *Adv. Mater.* **2008**, *20*, 168–173.

[26] Park, W. J.; Shin, H. S.; Ahn, B. D.; Kim, G. H.; Lee, S. M.; Kim, K. H.; Kim, H. J. Investigation on doping dependency of solution-processed Ga-doped ZnO thin film transistor. *Appl. Phys. Lett.* **2008**, *93*, 083508.

[27] Kamiya, T.; Nomura, K.; Hosono, H. Origins of high mobility and low operation voltage of amorphous oxide TFTs: Electronic structure, electron transport, defects and doping. *J. Disp. Technol.* **2009**, *5*, 468–483.

[28] Jeong, S.; Ha, Y. G.; Moon, J.; Facchetti, A.; Marks, T. J. Role of gallium doping in dramatically lowering amorphous-oxide processing temperatures for solution-derived indium zinc oxide thin-film transistors. *Adv. Mater.* **2010**, *22*, 1346–1350.

[29] Kim, G. H.; Jeong, W. H.; Kim, H. J. Electrical characteristics of solution-processed InGaZnO thin film transistors depending on Ga concentration. *Phys. Status Solidi (a)* **2010**, *207*, 1677–1679.

[30] Noh, H.-K.; Chang, K. J.; Ryu, B.; Lee, W.-J. Electronic structure of oxygen-vacancy defects in amorphous In-Ga-Zn-O

semiconductors. *Phys. Rev. B* **2011**, *84*, 115205.

[31] Yao, J. K.; Xu, N. S.; Deng, S. Z.; Chen, J.; She, J. C.; Shieh, H.-P. D.; Liu, P.-T.; Huang, Y.-P. Electrical and photosensitive characteristics of a-IGZO TFTs related to oxygen vacancy. *IEEE. Trans. Electron Dev.* **2011**, *58*, 1121–1126.

[32] Zan, H. W.; Yeh, C. C.; Meng, H. F.; Tsai, C. C.; Chen, L. H. Achieving high field-effect mobility in amorphous indium-gallium-zinc oxide by capping a strong reduction layer. *Adv. Mater.* **2012**, *24*, 3509–3514.

[33] Johnson, M. C.; Aloni, S.; McCready, D. E.; Bourret-Courchesne, E. D. Controlled vapor–liquid–solid growth of indium, gallium, and tin oxide nanowires via chemical vapor transport. *Cryst. Growth Des.* **2006**, *6*, 1936–1941.

[34] Vomiero, A.; Ferroni, M.; Comini, E.; Faglia, G.; Sberveglieri, G. Insight into the formation mechanism of one-dimensional indium oxide wires. *Cryst. Growth Des.* **2010**, *10*, 140–145.

[35] Schmidt, V.; Senz, S.; Gösele, U. Diameter dependence of the growth velocity of silicon nanowires synthesized via the vapor-liquid-solid mechanism. *Phys. Rev. B* **2007**, *75*, 045335.

[36] Fröberg, L. E.; Seifert, W.; Johansson, J. Diameter-dependent growth rate of InAs nanowires. *Phys. Rev. B* **2007**, *76*, 153401.

[37] Gao, T.; Wang, T. H. Catalytic growth of $In_2O_3$ nanobelts by vapor transport. *J. Cryst. Growth* **2006**, *290*, 660–664.

[38] Yang, Z.-X.; Wang, F. Y.; Han, N.; Lin, H.; Cheung, H.-Y.; Fang, M.; Yip, S.; Hung, T.; Wong, C.-Y.; Ho, J. C. Crystalline GaSb nanowires synthesized on amorphous substrates: From the formation mechanism to p-channel transistor applications. *ACS Appl. Mater. Interfaces* **2013**, *5*, 10946–10952.

[39] Yang, Z.-X.; Han, N.; Fang, M.; Lin, H.; Cheung, H.-Y.; Yip, S.; Wang, E.-J.; Hung, T.; Wong, C.-Y.; Ho, J. C. Surfactant-assisted chemical vapour deposition of high-performance small-diameter GaSb nanowires. *Nat. Commun.* **2014**, *5*, 5249.

[40] Rao, C. N. R.; Kulkarni, G. U.; Thomas, P. J.; Edwards, P. P. Size-dependent chemistry: Properties of nanocrystals. *Chem.—Eur. J.* **2002**, *8*, 28–35.

[41] Volokitin, Y.; Sinzig, J.; de Jongh, L. J.; Schmid, G.; Vargaftik, M. N.; Moiseevi, I. I. Quantum-size effects in the thermodynamic properties of metallic nanoparticles. *Nature* **1996**, *384*, 621–623.

[42] Chen, M.; Wang, X.; Yu, Y. H.; Pei, Z. L.; Bai, X. D.; Sun, C.; Huang, R. F.; Wen, L. S. X-ray photoelectron spectroscopy and auger electron spectroscopy studies of Al-doped ZnO films. *Appl. Surf. Sci.* **2000**, *158*, 134–140.

[43] Kumar, V.; Swart, H. C.; Ntwaeaborwa, O. M.; Kroon, R. E.; Terblans, J. J.; Shaat, S. K. K.; Yousif, A.; Duvenhage, M. M. Origin of the red emission in zinc oxide nanophosphors. *Mater. Lett.* **2013**, *101*, 57–60.

[44] Yerushalmi, R.; Jacobson, Z. A.; Ho, J. C.; Fan, Z. Y.; Javey, A. Large scale, highly ordered assembly of nanowire parallel arrays by differential roll printing. *Appl. Phys. Lett.* **2007**, *91*, 203104.

[45] Lee, J. S.; Chang, S.; Koo, S.-M.; Lee, S. Y. High-performance a-IGZO TFT with $ZrO_2$ gate dielectric fabricated at room temperature. *IEEE Electron Dev. Lett.* **2010**, *31*, 225–227.

[46] Nomura, K.; Takagi, A.; Kamiya, T.; Ohta, H.; Hirano, M.; Hosono, H. Amorphous oxide semiconductors for high-performance flexible thin-film transistors. *Jpn. J. Appl. Phys.* **2006**, *45*, 4303.